PAPER

Check for updates

Mechanistic insights into multimetal synergistic and electronic effects in a hexanuclear iron catalyst with a [Fe₃(μ₃-O)(μ₂-OH)]₂ core for enhanced water oxidation†

Zhi-Kai Shen,‡[a] Kang Li,‡[b] Zi-Jian Li,[a] Yong-Jun Yuan, [ID] [c] Jie Guan, [ID] *[b]
Zhigang Zou[a] and Zhen-Tao Yu [ID] *[a]

Multinuclear molecular catalysts mimicking natural photosynthesis have been shown to facilitate water oxidation; however, such catalysts typically operate in organic solutions, require high overpotentials and have unclear catalytic mechanisms. Herein, a bio-inspired hexanuclear iron(III) complex **I**, $Fe_6(μ_3-O)_2(μ_2-OH)_2(bipyalk)_2(OAc)_8$ (H_2bipyalk = 2,2′-([2,2′-bipyridine]-6,6′-diyl)bis(propan-2-ol); OAc = acetate) with desirable water solubility and stability was designed and used for water oxidation. Our results showed that **I** has high efficiency for water oxidation *via* the water nucleophilic attack (WNA) pathway with an overpotential of only *ca.* 290 mV in a phosphate buffer of pH 2. Importantly, key high-oxidation-state metal–oxo intermediates formed during water oxidation were identified by *in situ* spectroelectrochemistry and oxygen atom transfer reactions. Theoretical calculations further supported the above identification. Reversible proton transfer and charge redistribution during water oxidation enhanced the electron and proton transfer ability and improved the reactivity of **I**. Here, we have shown the multimetal synergistic and electronic effects of catalysts in water oxidation reactions, which may contribute to the understanding and design of more advanced molecular catalysts.

1 Introduction

The water-splitting reaction for hydrogen generation is potentially an efficient method to realize the goal of carbon neutrality.[1] However, applications of this reaction are largely limited by the sluggish water oxidation half-reaction.[2] Oxidizing water to molecular oxygen has unfavorable thermodynamics and requires overcoming a large kinetic barrier involving the transfer of four electrons and four protons.[3,4] These complex processes are conducted efficiently by multinuclear $CaMn_4O_5$ clusters in photosystem II (PSII) with a change in the protonation state of the bridging oxygen to facilitate successive oxidation steps without a prohibitive potential increase.[5,6] Furthermore, this unique natural catalyst can scatter the accumulated charge on the four Mn atoms through multimetal synergy to achieve a high oxidation state that promotes O–O bond formation during water oxidation.[7] This natural event involving the synergistic effect of multimetal centers is an ideal prototype template for research on artificial water splitting.[8] Artificial water oxidation catalysts based on the noble metals Ru[9] and Ir[10] have been proven to have high activity and stability. However, owing to the low abundance of noble metals, noble-metal-free catalysts are now essential. Despite some progress on Mn,[11] Co[12] and Cu,[13] a limiting feature is their lability, particularly in acidic media. Over the years, there has been some research progress on activity and stability of these catalysts.[14] Acidic solutions are the preferred media for water electrolysis because their high proton concentrations facilitate hydrogen production.[15] However, water oxidation in acidic media suffers from sluggish reaction kinetics. Therefore, developing active and durable multinuclear metal water-oxidation electrocatalysts for use in acidic solution is highly desirable.

Iron plays important roles in biology, including the transport and storage of O_2 in heme, and catalytic nitrogen reduction in nitrogenase (Fe₇Mo cluster).[16] Recently, a few

[a]*National Laboratory of Solid State Microstructures and Jiangsu Provincial Key Laboratory for Nanotechnology, College of Engineering and Applied Sciences, Nanjing University, Nanjing, Jiangsu 210093, People's Republic of China.
E-mail: yuzt@nju.edu.cn*
[b]*School of Physics, Southeast University, Nanjing, Jiangsu 211189, People's Republic of China. E-mail: guanjie@seu.edu.cn*
[c]*College of Materials and Environmental Engineering, Hangzhou Dianzi University, Hangzhou, Zhejiang 310018, People's Republic of China*

‡These authors contributed equally to this work.

polyiron complexes have been reported as electrocatalysts in water oxidation. Masaoka and coworkers studied three pentanuclear iron complexes in a neutral acetonitrile/water mixture and achieved high water oxidation activity exceeding that in nature.[17] Sokolov and coworkers investigated the activity of a hexanuclear iron cluster in neutral and basic borate buffer solutions.[18] In the multielectron transfer water oxidation reaction, charge accumulation and distribution on multiple iron atoms effectively cause multiple redox states and encourage O–O bond formation.[19] High-oxidation-state metal–oxo intermediates are often indispensable in water oxidation and require stabilization by an appropriate ligand design.[20] However, many critical issues regarding the use of multinuclear catalysts remain unresolved, including the use of organic solvents as electrolytes and the formation of heterogeneous active species during water oxidation.[21] In this regard, it is necessary to develop multinuclear iron-based molecular water oxidation catalysts with high efficiency and good stability in acidic aqueous solutions.

In this study, we designed and synthesized a water-soluble hexanuclear iron(III) complex I, $Fe_6(\mu_3\text{-}O)_2(\mu_2\text{-}OH)_2$ (bipyalk)$_2$(OAc)$_8$ (H$_2$bipyalk = 2,2′-([2,2′-bipyridine]-6,6′-diyl)bis (propan-2-ol); OAc = acetate). A bipyalk ligand with strong electron-donating groups can improve the stability of high-oxidation-state intermediates formed during water oxidation.[12] Complex I exhibits outstanding water oxidation activity and stability under acidic conditions (TOF of 2.9 s^{-1}). The high-oxidation-state Fe^{IV}=O intermediates formed during water oxidation are directly observed through *in situ* spectroelectrochemistry as well as oxygen atom transfer experiment, and confirmed by the TD-DFT-calculated electronic absorption spectrum. The WNA mechanism is the most promising pathway for water oxidation under acidic and neutral conditions, as proven by kinetics studies and supported by density functional theory (DFT). Furthermore, DFT calculations indicate that the multimetal synergy in complex I can reduce the free energy barrier to boost the water oxidation activity, which is structurally and electronically mediated through reversible proton transfer on μ_2-OH and charge redistribution. This study promotes the understanding of the catalytic mechanism in water oxidation, and provides crucial insights into the design of high-perform-

ance multinuclear molecular electrocatalysts. Furthermore, this multinuclear iron-based molecular catalyst could be used as a model to gain a deeper understanding of the catalytic mechanism of heterogeneous iron oxides.

2 Results and discussion

2.1 Catalyst characterization

Single-crystal X-ray diffraction analysis demonstrated that complex I is a centrosymmetric hexanuclear iron complex as shown in Fig. 1a. The crystallographic data for complex I are presented in Table S1.† These six Fe(III) atoms in complex I are composed of two isosceles triangular $[Fe_3(\mu_3\text{-}O)]^{7+}$ units bridged by two μ_2-OH and four acetate groups (Fig. 1b), unlike the edge-sharing connected $[Fe_3(\mu_4\text{-}O)]^{7+}$ in the hexanuclear iron complex synthesized by the Sokolov group.[18] Furthermore, the two μ_2-OH groups are on opposite sides of the mean plane through the six iron atoms, which is different from the hexanuclear iron complexes synthesized by the Lippard group, forming a twisted boat conformation with both hydroxo bridges pointed toward the same side.[22,23] The Fe–O distances and Fe–O–Fe bond angle support the presence of a hydroxo bridge in Fe–(μ_2-O)–Fe units, consistent with reported structures bearing μ-OH units.[24,25] This assignment was further supported by the FT-IR spectrum of complex I (Fig. S2a†); the vibrations of bridging OH groups (μ_2-OH) and O groups (μ_3-O) were observed *ca.* 1135 cm^{-1} and 806 cm^{-1}, respectively.[26–28] During water oxidation, the hexacoordinated centers are more likely to be attacked by water molecules than the heptacoordinated species.[29] In addition, the coordinated acetate ions interacts strongly with water molecules, increasing water solubility and decreasing barriers to water oxidation,[30] which are essential characteristics of an effective molecular water oxidation catalyst.

The presence of the hexanuclear iron core of complex I was established using electrospray ionization-mass spectrometry (ESI-MS, Fig. S2b†). The prominent ion peaks of complex I in methanol at mass-to-charge (m/z) ratios of 701.4911 and 475.3239 with an isotopic pattern are attributed to the doubly ([M − OAc$^-$ + 2H$^+$ + 2Na$^+$]$^{2+}$, calculated m/z of 701.4829) and
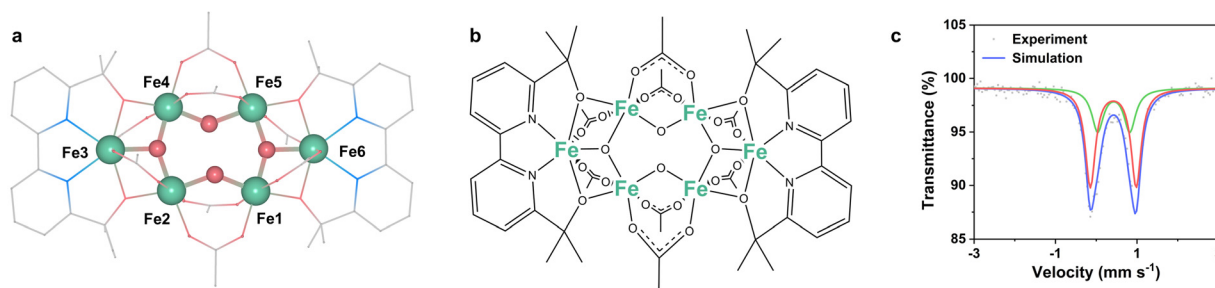

Fig. 1 (a) X-ray crystal structure and (b) schematic representation of the molecular structure of complex I. Color scheme: Fe (green), O (red), N (blue), and C (gray); all hydrogens are omitted for clarity. (c) ^{57}Fe Mössbauer spectroscopy of complex I. Color scheme: simulation (blue), doublet I (D1, red), doublet II (D2, green).

triply ([M − OAc⁻ + 2H⁺ + 3Na⁺]³⁺, calculated m/z of 475.3184) charged fragments of complex **I**, respectively. The corresponding ions were also observed in water (m/z 701.4913 and 475.3244). The iron oxidation state may change during the electrospray process,[31] which is supported by the LOBA results (Fig. S2c†). The high-phase purity of complex **I** was also confirmed using powder X-ray diffraction (Fig. S3a†). The [57]Fe Mössbauer spectrum clearly reveals the presence of two slightly different iron(III) sites (Fig. 1c, the velocity was calibrated relative to α-iron). In addition, the spectrum was fitted with two symmetric quadrupole doublets with area ratio of 2 : 1, coinciding with the isosceles triangular $[Fe_3(\mu_3\text{-}O)]^{7+}$ geometry in complex **I**. The two quadrupole doublet distributions have similar isomer shifts (IS) of 0.41 and 0.43 mm s⁻¹, but are distinguished by their average quadrupole splittings (QS), centered at 1.12 and 0.77 mm s⁻¹ for D1 and D2, respectively. Similar isomer shifts of the two iron sites are typical of iron(III) in a trinuclear μ-oxido iron(III) complex.[32] The difference in quadrupole splitting between the Fe sites arises from the different coordination environments between FeO_6 and FeO_5N_2 sites.[33] Additionally, the Mössbauer spectrum indicates the presence of high spin Fe ($S = 5/2$) in complex **I**.[34] The observed $\chi_M T$ at room temperature is 9.7 cm³ K mol⁻¹, which is less than the expected value of this spin assignment (Fig. S3b†). The reason is probably that the magnetic moment is considerably affected by the coordination sphere and the antiferromagnetic between the hexanuclear iron atoms.[18] Similar results have been reported based on multinuclear oxo-bridged Fe(III) systems.[33,35]

2.2 Water oxidation performance studies

Owing to advantageous water solubility of complex **I**, its water oxidation performance in aqueous phosphate buffer was explored using cyclic voltammetry (CV). According to related reports, buffer ions (*e.g.*, phosphate buffer) may act as proton acceptors during water oxidation (Fig. S4a†), which plays a vital role in boosting the catalyst activity.[36] As shown in Fig. 2a, the catalytic waves from the ligand solution and blank phosphate buffer are negligible, while the irreversible anodic current in complex **I** is clearly enhanced compared to that in the background, which is attributable to the water oxidation process. These results demonstrate that complex **I** engaged effectively in water oxidation. Although, the required oxidation of iron was not observed for the signal overlap with the water oxidation current, it was proven by differential pulse voltammetry (DPV, Fig. 2b) measurements.[37] This redox behavior is in line with the wave obtained in an anhydrous acetonitrile (N₂-saturated, Fig. S4b†) that have been assigned to the Fe[III/IV] couple according to previous report.[38] The occurrence of reversible proton transfer on μ₂-OH within our proposed water oxidation cycle (as discussed later) may account for the observation of only one oxidation peak in both the CV and DPV results.[5,39] Upon adding 5% H₂O to the acetonitrile solution of complex **I**, the oxidation current considerably increased (Fig. S4c†), consistent with an electrocatalytic water oxidation process. Importantly, complex **I** exhibited significant catalytic
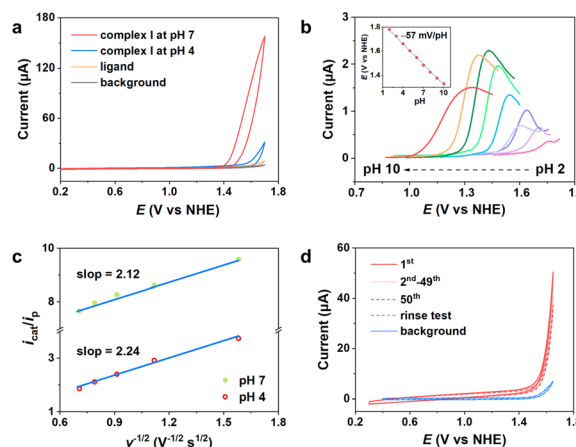
Fig. 2 (a) CVs of complex **I** in pH 4 and pH 7 phosphate buffer, ligand and blank electrolyte. Voltammograms were collected on a glassy carbon (GC, 0.07 cm²) electrode at a scan rate of 50 mV s⁻¹. (b) DPV curves of complex **I** in phosphate buffer of different pH values; Inset: corresponding Pourbaix diagram. (c) Plots of the ratio of i_{cat} to i_p as a function of the inverse of the square root of the scan rate v, showing a linear relation. (d) CVs of complex **I** (0.25 mM) in a phosphate buffer (pH 4, 50 cycles, 1 cm² FTO electrode, 50 mV s⁻¹). Blue solid line: the electrode after 50 scans followed by rinsing and replacement in a fresh background solution; blue dashed line: fresh electrode in blank pH 4 phosphate buffer.

current in phosphate buffers of pH 2–6 (Fig. 2a and Fig. S4d†), implying that complex **I** is a suitable water oxidation catalyst for use in acidic conditions. The catalytic current increased with increasing pH because the reaction is thermodynamically favorable under high pH conditions.[40] The significant change of catalytic current at pH values below 5 may be related to protonation of the hydroxyl functionality of **I**. The experimental pK_a values of complex **I** were found to be p$K_{a1} \approx 4.0$ and p$K_{a2} \approx 4.8$, respectively (Fig. S5a†). The DFT calculations suggest that the protonation of a bridging OH is energetically more unfavorable (by 0.03 eV) than that at the terminal site of cleavage of a bridging acetate group (Fig. S5b–d†). The pK_a values of various intermediates were calculated according to the literature,[41,42] see below.

To elucidate the water oxidation kinetics of complex **I**, CVs of complex **I** at different catalyst concentrations and various scan rates were performed at pH 4 and pH 7 (Fig. S6 and S7†). The catalytic currents varied linearly with the catalyst concentrations, indicating that the catalytic process involved a single-molecule catalytic species (the inset in Fig. S6 and S7†).[43] In addition, the first-order relation between the peak current (i_p) and square root of the scan rate ($v^{1/2}$) indicated the presence of a diffusion-controlled electrocatalytic process (Fig. S6 and S7†).[44] These results were consistent with the catalytic mechanism suggested by DFT calculations, as discussed later. By plotting i_{cat}/i_p *versus* $v^{-1/2}$, the k_{cat} (TOF) of complex **I** was calculated to be *ca.* 2.4 s⁻¹ for pH 4 and 2.2 s⁻¹ for pH 7 using eqn (S5)† (Fig. 2c), both slightly smaller than those calculated later in FOWA (*ca.* 2.9 s⁻¹ and 2.8 s⁻¹ for pH 4 and pH 7,

respectively). The Tafel slope for complex **I** was *ca.* 75 mV dec^{-1} and *ca.* 78 mV dec^{-1} under pH 4 and pH 7, respectively (Fig. S8 and Table S2†). These results show that complex **I** exhibits high catalytic activity for electrocatalytic water oxidation (even under acidic conditions), surpassing that of well-known Fe-based catalysts (compared in Table S3†).

To gain further insights into the mechanism of O$_2$ production in water, the electrocatalytic capacity of complex **I** for water oxidation at pH 2–10 in phosphate buffered aqueous medium was studied (Fig. 2b and Fig. S4d†). The inset in Fig. 2b shows the *E*–pH relationship (Pourbaix diagram) from DPV measurements. The oxidation waves were pH-dependent with a Nernstian slope of −57 mV per pH, corresponding to that of a proton-coupled electron transfer (PCET) process.[45] The one-electron nature of the redox event was further confirmed by the CPE experiment (Fig. S11c†).[46] In a pH range of 6–10, the relationship between onset potentials of catalytic oxidation and pH of the examined aqueous solutions exhibited a Nernstian slope of −56 mV per pH, consistent with the 1H$^+$/1e$^-$ procedure in the Pourbaix diagram.[47] The CVs of complex **I** in different pH phosphate buffers showed that complex **I** can catalyze water oxidation in acidic aqueous solution with a small onset potential of ac. 290 mV (pH 2), further indicating that complex **I** is a suitable catalyst for acidic water oxidation. This overpotential was lower than that of previously reported Fe-based molecular compounds under acidic conditions (Table S3†).[48]

2.3 Catalyst integrity studies in water oxidation

For water oxidation to proceed, the catalysts require providing coordination sites for water molecules to access the inner sphere of metal ions.[49] In this way, structural integrity of molecular catalysts during the removal of the coordination ligands is a critical issue, especially under harsh reaction conditions.[50] Therefore, it is very important to identify the active species probably arising from the transformation of the initial molecule for understanding catalysis.[51]

Firstly, the structural stability of complex **I** in aqueous buffer was verified by spectroscopic studies. The NMR spectra at pH 2 in phosphate-buffered D$_2$O was comparable to that in neat D$_2$O (Fig. S9†). After 72 h, no insoluble product was found (considering the solubility of H$_2$bipyalk), indicating that no decomposition of complex **I** occurs in acid conditions. The presence of acetate groups on complex **I** is indicated by a distinctive IR peak at *ca.* 1275 cm^{-1} (Fig. S10a–c†),[52] which remained almost unchanged in different pH conditions. The pH-dependent UV–Vis spectrum (Fig. S10e†) shows two strong absorption bands at 235 nm to 310 nm, corresponding to the L–π → L–π* transitions of the aromatic bipyalk ligand (L). The TD-DFT-calculated electronic absorption spectrum of complex **I** is in good agreement with the experimental observations (Fig. S10f†). The UV–Vis spectra of complex **I** remained unchanged over time (throughout 72 h) in phosphate buffer (Fig. S10g†), showing that complex **I** is sufficiently stable for use as a water oxidation catalyst. The Raman spectra (Fig. S10d†) also showed that complex **I** is sufficiently stable for use as a water oxidation catalyst. These results suggest that the main structure of the complex is maintained under these conditions. However, complex decomposition is complex and may not be excluded under more long-time oxidation reaction and stronger acidic conditions (pH ≤ 2).[21]

Under catalytic conditions, the stability of complex **I** and its possible deposition were evaluated by control experiments and spectroscopic techniques. Multiple successive CV scans were performed in phosphate buffer with 0.25 mM complex **I** using FTO (fluorinated tin oxide, with an exposed area of 1 cm^2) as the working electrode. After 50 cycles, the catalytic current in pH 4 phosphate buffer slightly decreased (Fig. 2d), while the CV curves in pH 7 phosphate buffer almost overlapped (Fig. S11a†). After multiple CV scans and long-term constant potential electrolysis (CPE), the electrode was rinsed with deionized water and recycled in a fresh buffer solution without catalyst. No discernible catalytic activity was observed after recycling compared with the initial background CV curve (Fig. S11a and b†). Stable catalytic current and inactive electrode after CPE suggest that no FeO$_x$ nanoparticles or film formed at the surface of the electrode,[21] which also might not be detected due to the weakly adsorption of the decomposition components.[51] During long-term CPE (Fig. S11b†) at 1.70 V *vs.* NHE, the current first slightly decreased and then remained almost constant for 5 h at pH 2. The surface compositions of the FTO electrode and phosphate buffer containing complex **I** after CPE were further investigated. In DLS analysis (dynamic light scattering, Fig. S11d†), no heterogeneous nanoparticles in the phosphate buffer were detected after water oxidation. The concentrations of Fe ions in the phosphate buffer containing complex **I** did not change before and after the CPE, as confirmed by inductively coupled plasma optical emission spectroscopy (ICP-OES, Table S4†), indicating that complex **I** was not decomposed during water oxidation. According to X-ray photoelectron spectroscopy (XPS, Fig. S12a–c†) analysis, no new species were deposited on the electrode surface during water oxidation by comparing the spectra of the immersed FTO electrode (no voltage applied) and blank FTO. The SEM and UV–Vis analysis (Fig. S12d–f†) of the FTO electrodes also confirmed the homogeneous catalysis process. To further rule out the formation of catalytically active surface deposits, electrochemical quartz crystal microbalance (EQCM) experiments were carried out in pH 4 and 7 phosphate buffer. The results show no significant change in the oscillation frequency of the electrode in the presence of complex **I** (Fig. 3a and S13a†), which indicates that catalytically active species stay homogeneous and suggests that they are molecular in nature. The formation of heterogeneous species (*e.g.*, FeO$_x$, Fe(PO$_4$)$_x$) depends on the solution conditions, especially the pH value. The current results support the molecular nature of complex **I** and its good stability (under the current operation) during water oxidation at low pH values as proposed with the Fe complexes by Lau, Fukuzumi *et al.*,[53,54] which was further corroborated by differential electrochemical mass spectrometry (DEMS, see below).
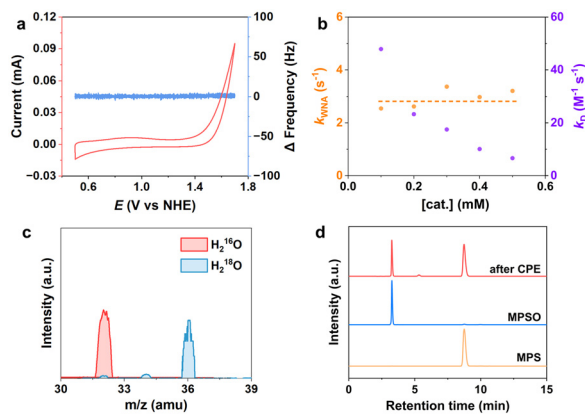
Fig. 3 (a) Results of EQCM experiment of 0.25 mM complex **I** in pH 4 phosphate buffer. (b) Plot of calculated k_D and k_{WNA} vs. [cat.] for FOWA at pH 4. (c) DEMS signals of O_2 products during water oxidation (1.70 V vs. NHE) by complex **I** (0.25 mM) in phosphate buffer (pH 7) containing $H_2^{16}O$ and $H_2^{18}O$ (97 atom% ^{18}O). (d) High-performance liquid chromatography (HPLC) profiles of electrolyte (acetonitrile, with 5% H_2O, 0.1 M Et_4NClO_4 and 1 mM MPS) after CPE (1.70 V vs. NHE) for 2 h.

2.4 Water oxidation mechanistic studies

As shown in Fig. S13b,† the catalytic performances of complex **I** in both H_2O and D_2O were studied, yielding a calculated kinetic isotope effect (KIE) value of ca. 2.0, which suggests that O–H bond cleavage is involved in the rate-determining step (RDS) of water oxidation, which is consistent with the characteristics of a WNA mechanism.[55] The kinetic performance of complex **I** was evaluated by foot of the wave analysis (FOWA) based on catalytic water oxidation waves, as shown in Fig. 3b and Fig. S14.† The observed reaction rate constant k_{WNA} remained almost unchanged at different concentrations of complex **I** at both pH 4 and pH 7, which is suggestive of the first-order dependence of the catalytic reaction kinetics for potential reaction mechanism.[56]

The O_2 evolved during the CPE experiment was quantified to be ca. 6 μmol (pH 2) and ca. 75 μmol (pH 7) using gas chromatography, respectively. The maximum faradaic efficiency and turnover number of water oxidation catalyzed by complex **I** was measured as ca. 94% and 30, respectively. Rotating ring–disk electrode (RRDE, Fig. S15a†) measurements revealed that no current of H_2O_2 oxidation was observed at the Pt ring electrode, indicating highly selective oxidation of water to oxygen by complex **I**.[12] To confirm the source of oxygen, differential electrochemical mass spectrometry (DEMS) was performed to measure the O_2 generated during water oxidation (1.70 V vs. NHE) by complex **I** in phosphate buffer (pH 7) containing $H_2^{16}O$ and $H_2^{18}O$ (97 atom% ^{18}O). Fig. 3c indicates that both oxygen atoms in the evolved O_2 are generated from water. Under alkaline conditions, the oxygen source for O–O bond formation may be quite different according to previous reports.[57] The catalytic ability and stability of complex **I** under acidic conditions were demonstrated by DEMS. As shown in Fig. S15b,† the evident O_2 signal supports that complex **I** can catalyze water oxidation to release O_2 even at pH 2, which was

also confirmed by gas chromatography. In addition, no CO_2 was detected, demonstrating that acetate groups in complex **I** without being oxidized and that molecular nature of the catalytic process under these oxidative conditions.

The in situ spectroelectrochemistry of complex **I** was extensively studied to elucidate the reaction kinetics and mechanism. In a blank phosphate buffer, no new absorption peak was detected at the catalytic voltage (1.70 V vs. NHE, Fig. S16a†). The time-dependent absorbance of complex **I** at a constant potential showed no change in the UV range (Fig. S16b).† Evidence of the formation of water oxidation intermediates was observed in the visible range, and a weak band at 637 nm emerged (Fig. S16c†), which was assigned to high-oxidation-state $Fe^{IV}=O$ intermediates. This result was consistent with the previous study on Fe-based water oxidation[58] and further confirmed by the TD-DFT-calculated electronic absorption spectrum (Fig. S16d†). The calculated absorption peak at approximately 620 nm was contributed by electron excitation from O (the first attack water molecule)-2p to Fe-3d, and intra-atomic Fe 3d–3d transitions. When electrolysis was stopped, the spectrum reverted back to the initial state before the potential was applied, indicating high stability of the catalyst. Conversely, the absorption spectrum of complex **I** remained unchanged at 1.30 V vs. NHE (Fig. S16e†), consistent with the CV results in which no water oxidation signal appeared at this voltage. Specifically oxidation of methyl phenyl sulfide (MPS) to methyl phenyl sulfoxide (MPSO) via an oxygen atom transfer reaction is one of the characteristic features of $Fe^{IV}=O$ species.[59] The oxidation product MPSO was detected in the electrolyte after CPE for 2 h by high-performance liquid chromatography (HPLC, Fig. 3d), demonstrating the formation of $Fe^{IV}=O$ intermediates during water oxidation. For comparation, no $Fe^{IV}=O$ species could be generated in blank electrolyte and in the presence of a Fe salt (Fig. S16f†).

2.5 Density functional theory (DFT) calculations and theoretical analysis

2.5.1 Reversible proton transfer in water oxidation. The mechanism of the catalytic process was further investigated by DFT calculations. Hettersheid and coworkers proposed that O–O bond forms via a SET-HA (single-electron transfer hydroxide attack) mechanism, and the utilization of redox-active ligands facilitates the ability to delocalize an electron in the π system of the ligand without the need to raise the oxidation state of the metalcenter.[60] Bernhard, Collins and coworkers reported that Fe-TAML (tetraamido macrocyclic ligand) can efficiently catalyzes the oxidative conversion of water to dioxygen via $Fe^{IV}–O–Fe^{IV}$ dimer intermediate, and improved catalyst performance was associated with increasingly electron-withdrawing substituents on the TAML.[61] Lloret-Fillol and coworkers proved the kinetic unviability of mononuclear $Fe^{IV}(O)$ species to perform the O–O bond formation event at room temperature by theoretical calculations because of the high endergonic nature of the intermediates formed after the O–O bond formation.[62] They also pointed out that introduction of an internal base in iron complex can reduces the energy of the O–

O bond formation barrier. So, this gives us more inspiration to explore the detail of water oxidation mechanism of complex **I**, as well as encourages us to explore whether the O–O bond formation can be achieved through intramolecular proton transfer with low activation free energy.

As all the intermediates and their corresponding free energy changes are shown in Fig. 4, three possible water oxidation pathways were considered: path **1** and path **2** for the water nucleophilically attack mechanism (WNA)[12] and path **3** for the intramolecular oxo/oxo coupling mechanism. As shown in Fig. S17a and b,† after Fe1 in **I** is nucleophilically

attacked by the first H_2O, the bridging acetate ligand changes its coordination mode from bidentate to monodentate.[63] The **Fe^{III}–OH–Fe^{III}–OH$_2$** species (**II**) is formed with a lower free energy change by breaking of the Fe1–O3 bond ($\Delta G = 0.56$ eV, Fig. S18†) instead of breaking of the Fe1–O5 bond ($\Delta G = 0.79$ eV). The longer bond distance of Fe1–O3 (O3 of C–O in acetate ligand, 2.041 Å) affords a lower bond energy than Fe4–O4 (O4 of C=O in acetate ligand, 2.027 Å). These results indicate that Fe1–O3 is more likely to break to form **II** and thus initiate the catalytic cycles. Then **II** undergoes a PCET process to form **Fe^{III}–OH–Fe^{IV}–OH** species (**III**) ($\Delta G = 0.49$
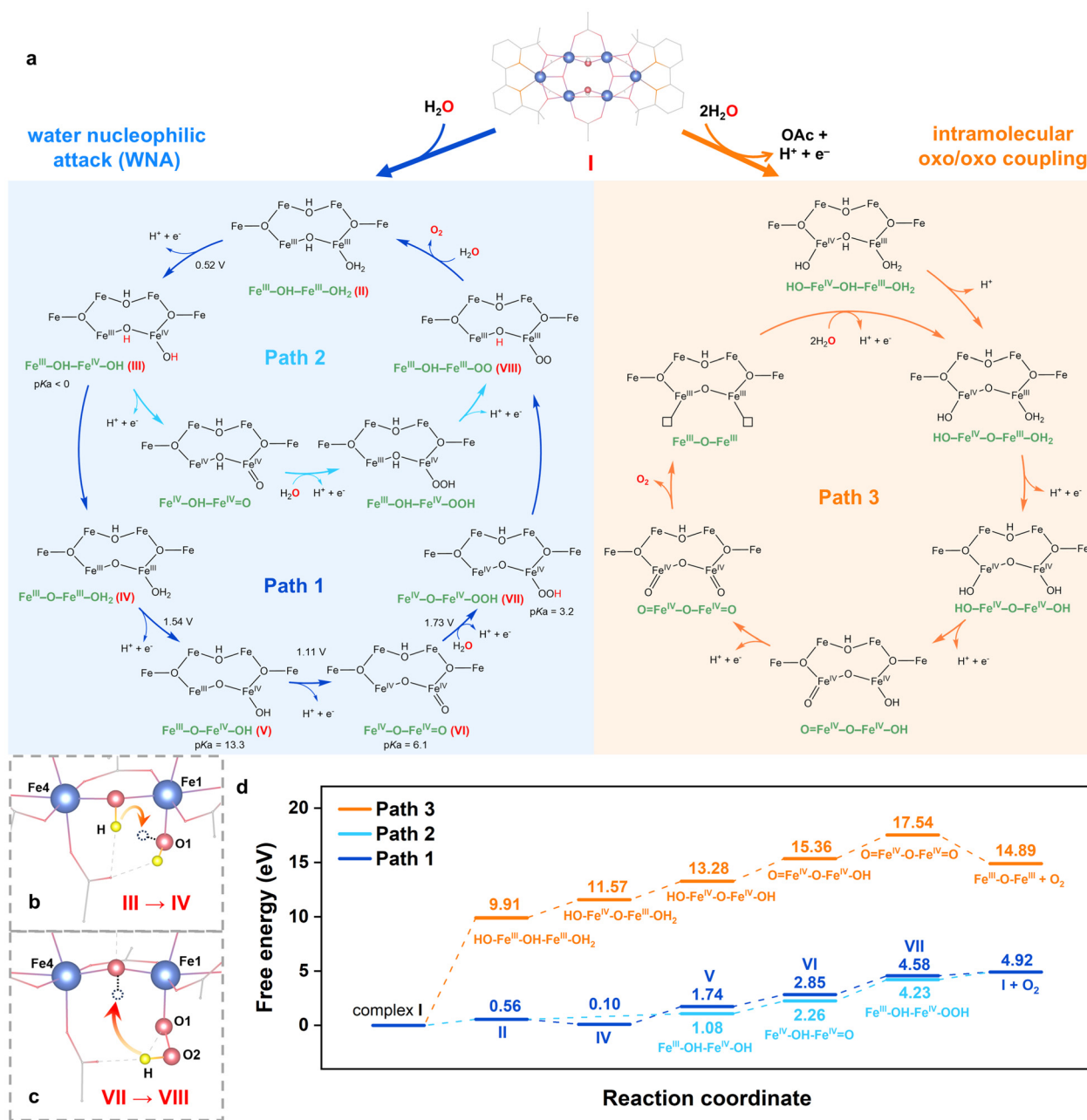

Fig. 4 (a) Possible schematic of the proposed catalytic cycles by complex **I**. Intramolecular proton transfer during (b) **III → IV**, and (c) **VII → VIII**. (d) Energy diagram for the proposed water oxidation cycles with the Fe$_6$ model complex **I**.

eV). Accordingly, two possible pathways are considered for the reaction to proceed from **III** to the superoxo species **Fe^{III}–OH–Fe^{III}–OO** (**VIII**).

In path **1**, the catalytic cycle ensues that **III** undergoes intramolecular proton transfer from the bridging hydroxide (μ_2-OH between Fe1 and Fe4) to the –OH on Fe1 (Fig. 4b), and affords **Fe^{III}–O–Fe^{III}–OH$_2$** species (**IV**) ($\Delta G = -0.46$ eV). In this step, oxidation state of Fe1 changes from IV to III, while oxidation state of Fe3 changes from III to IV. Subsequently, two consecutive one-electron transfers coupled with proton transfer occur to afford **Fe^{III}–O–Fe^{IV}–OH** species (**V**) and then reactive **Fe^{IV}–O–Fe^{IV}=O** species (**VI**). The calculated free energy increase for these two steps are 1.64 eV and 1.11 eV, respectively. The formation of a key high-oxidation-state Fe^{IV}=O intermediate (species **VI**) was identified by *in situ* spectroelectrochemistry results (Fig. S16c†) and was supported by the TD-DFT-calculated electronic absorption spectrum (Fig. S16d†) as discussed above. In addition, the Fe1–O1 bond in **VI** (1.654 Å) is shorter than that in **V** (1.801 Å), indicating that a Fe1=O1 double bond may be formed after deprotonation, consistent with the charge distribution results discussed later. Species **VI** undergoes another water nucleophilic attack on the Fe^{IV}=O oxyl species to generate hydroperoxo **Fe^{IV}–O–Fe^{IV}–OOH** intermediates (**VII**) ($\Delta G = 1.73$ eV), which turns out to be the rate-limiting step in the catalytic cycle. In **VII**, the presence of the relatively weak peroxy bond results in relatively low stability and therefore in the highest energy necessary for O–O bond formation during the catalytic cycle. Afterward, species **VII** undergoes intramolecular proton transfer from –OOH back to the bridge oxygen atom (μ_2-O between Fe1 and Fe4) to yield **VIII** (Fig. 4c), overcoming a small activation barrier of only 0.12 eV. The deprotonation of bridging hydroxide as well as proton extraction by bridging oxide during the oxygen evolving transition in this process may be the key features of water oxidation in PSII.[64] Furthermore, the relatively long Fe1–O1 bond in **VII** (1.843 Å) and **VIII** (1.850 Å) indicates weak bond strength, facilitating the release of O$_2$ during water oxidation. Finally, Fe1 is attacked by a new H$_2$O, accompanied by the release of an O$_2$ molecule and the regeneration of **II** ($\Delta G = 0.34$ eV), thus restarting the catalytic cycle. In addition, in all the intermediates (except **VI**), a typical hydrogen bond is formed between H (from the attack water molecule) and dangling O (from the disconnected acetate ligand), which contributes to the good stability of the intermediates and may enhance the water oxidation performance.[65] The deprotonation of the bridging hydroxide in path **1** appears to be thermodynamically favorable for a dramatic free energy decrease of 0.46 eV from **III** to **IV**. In path **2**, no intramolecular proton transfer occurs. After the formation of III, three successive PCET processes take place, forming **Fe^{IV}–OH–Fe^{IV}=O** ($\Delta G = 1.21$ eV), **Fe^{III}–OH–Fe^{IV}–OOH** ($\Delta G = 1.97$ eV) and species **VIII** ($\Delta G = 0.47$ eV) intermediates. The O–O bond formation appears to be the rate-limiting step in the catalytic cycle with a large activation free energy of 1.97 eV, which is 0.24 eV greater than that in path **1**. Therefore, path **1** from **III** to **VIII** is more energetically accessible than path **2**.

A second possible mechanism of intramolecular oxo/oxo coupling within binuclear[19] and pentanuclear[17] iron complexes was considered (Fig. 4a, path **3**), which in different with WNA mechanism in path **1** and **2**. Complex **I** is simultaneously attacked by two H$_2$O molecules, and the acetate ligand is completely detached. The detached acetate ligand captures one H from H$_2$O and is divorced from the catalytic system. The remaining OH and the other H$_2$O then bind to the two exposed Fe atoms (Fe1 and Fe4) to form **HO–Fe^{IV}–OH–Fe^{III}–OH$_2$** ($\Delta G = 9.91$ eV). Throughout the oxidation process, each step of the intramolecular oxo/oxo coupling pathway (path **3**) has a relatively higher energy barrier than that of two WNA pathways. In addition, the extremely high energy ($\Delta G = 9.91$ eV) required for the desorption of the acetate ligand clearly reduces the thermodynamic feasibility of the intramolecular oxo/oxo coupling mechanism (path **3**) compared to the WNA mechanism. On the other hand, both the KIE (KIE ≈ 2.0) and catalytic behavior (catalytic currents varied linearly with varying catalyst concentrations) of complex **I** indicate that the intramolecular oxo/oxo coupling pathway of O–O bond formation *via* the diiron sites **O=Fe^{IV}–O–Fe^{IV}=O** or **O=Fe^{IV}–O–Fe^{V}=O** can be excluded.[19] Correspondingly, the catalytic process for complex **I** may follow a single-site reaction path for O–O bond formation involving the nucleophilic attack of an external water molecule and the formation of a high-oxidation-state iron–oxo intermediate, which is also supported by the FOWA techniques discussed above. Another possible pathway of water oxidation through H$_2$O insertion into the Fe1 center was found to be energetically less favorable without breaking the bond between Fe1 and the O in the acetate ligand, as shown in Fig. S19.† Thus, path **1**, *via* the WNA mechanism, is the most favorable for water oxidation by complex **I**, in terms of both DFT calculations and experimental results. It is worth pointing out that additional possible catalytic mechanisms involving a radical localized on the metal, buffer ions, *etc.*, may also contribute to the O–O bond formation.

2.5.2 Synergistic and electronic effects for enhancing water oxidation. The electronic structure of the intermediates in path **1** was investigated because it will considerably affect the water oxidation activity of the catalyst. The differential charge density ($\Delta\rho$) distribution (Fig. 5a–d) reveals the electronic character during the deprotonation processes. The deprotonation of bridging hydroxide (**II → IV**) coupled with a PCET process led to a clear electron transfer from the t_{2g} orbitals to e_g orbitals in both Fe1 and Fe4, indicating a higher spin polarization of Fe1 and Fe4 in the formed **IV**. After the first deprotonation of the attacking water molecule (–Fe1–OH$_2$ → –Fe1–OH), there was an electron accumulation on the σ-bonding orbital of Fe1–O1, indicating the presence of a stronger σ-bond in **V** (1.801 Å) than in **IV** (2.080 Å). The favorable e_g occupancy and stronger σ-bonds are beneficial to stabilize water oxidation intermediates.[65] In addition, the obvious charge redistribution in **IV** may maximize the Fe 3d–O 2p covalency in **V**, allowing complex **I** to serve as an active catalyst for water oxidation.[66] Subsequently, the second deprotonation of the attacking water molecule (–Fe1–OH → –Fe1=O) leads to the electron accumulation on
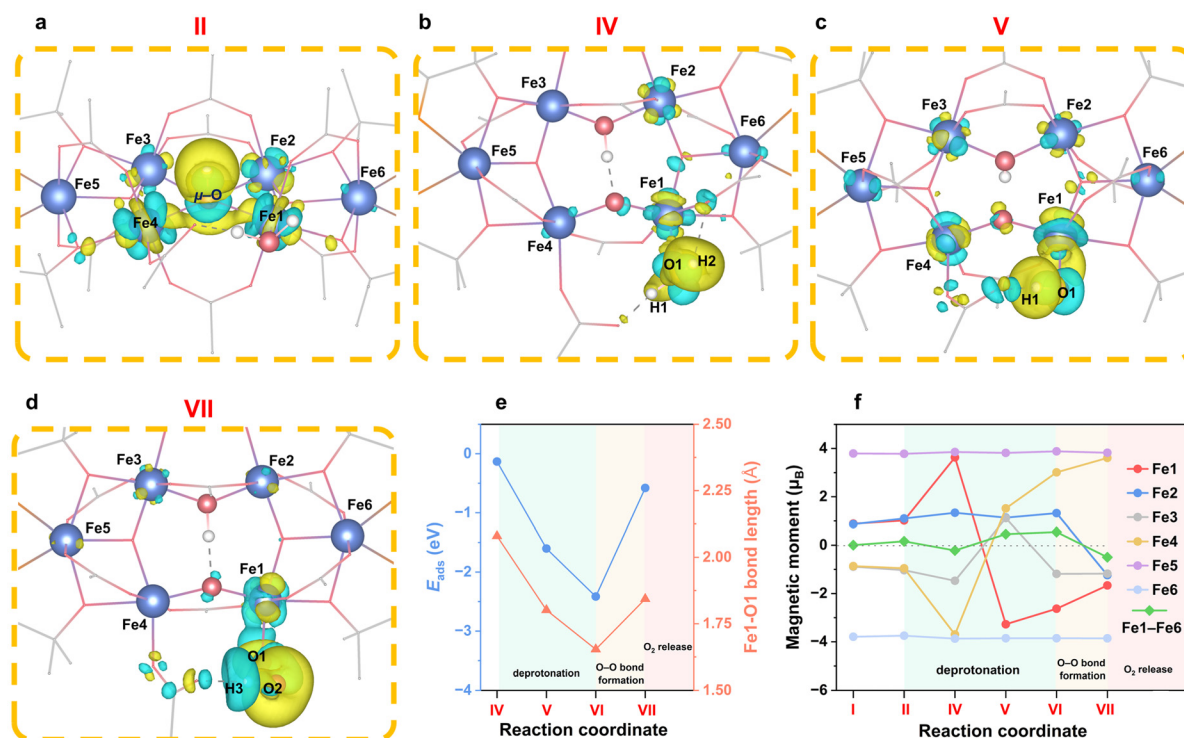
Fig. 5 Differential charge density distribution for (a) disconnecting H in the bridging hydroxide (μ_2-OH between Fe1 and Fe4) in **II**, (b) disconnecting H2 in **IV**, (c) disconnecting H1 in **V** and (d) absorbing the OH (−O2−H3) group in **VII**. Electron accumulation and depletion are represented by yellow and blue, respectively. Color scheme: Fe (blue), O (red), N (yellow), C (gray), and H (white); all hydrogens (except in water molecules and the bridging hydroxide) are omitted for clarity. The isosurface values are set to ± 0.005 e Bohr^{-3}. (e) Adsorption energy for the adsorbate (blue line) and the bond length of Fe1−O1 (orange line) in corresponding intermediates of path **1**. (f) Atomic magnetic moment (m) for six Fe atoms in pristine complex **I** and the intermediates of the WNA mechanism.

the t$_{2g}$ orbitals of Fe1 and the π-bonding states, indicating the formation of a σ and π double bond between Fe1 and O1 in **VI**. Finally, electron depletion around Fe1 shows that π-bonding disappears again when **VI** is attacked by the second H$_2$O to generate **VII**. In addition, the distinct $\Delta\rho$ near hydrogen (H1 in Fig. 5c, H3 in Fig. 5d) and the dangling O atom of the acetate ligand indicate that they are stabilized by the formation of a specific hydrogen bond in **V** and **VII**.[65] These charge redistributions in complex **I** as well as the orbital interaction between Fe1 and O1 could affect the bond strength (Fig. 5e) and water oxidation performance.[66] Furthermore, the oxygen adsorption energy (E_{ads}) in the key intermediates of path **1** is given (Fig. 5e) by the coupling of O 2p to the d electrons, which is a good descriptor for water oxidation.[67] The fluctuation trend of the adsorption energy is consistent with the change in the Fe1–O1 bond length in the structural analysis (Fig. S17†). This suitable tendency helps to stabilize water oxidation intermediates and promote the release of O$_2$, thereby ultimately enhancing the water oxidation performance.[68]

The electron transfers (accumulation and depletion) of the six Fe atoms in path **1** is studied by Bader charge analysis. The electron accumulation and depletion of the six Fe atoms (Fig. S20†) share a self-consistent tendency with the spin vari-

ation (Fig. 5f). Specifically, the Fe atoms lose more electrons with a corresponding increase in spin polarization. Notably, all the Fe atoms display electron depletion during the deprotonation of bridging hydroxide (**II** → **IV**), which indicates an increase in the electronegativity of Fe atoms, especially for Fe1 and Fe4. The higher electronegativity of Fe1 and Fe4 can activate bridge oxygen atom (μ_2-O between Fe1 and Fe4) as a proton acceptor to promote intramolecular proton transfer (**VII** → **VIII**).[65] Moreover, a similar "bridging hydroxide effect" has been proposed for the oxygen evolving complex of PSII, which may counteract the voltage increase in the subsequent required metal oxidation step.[39,69] The simultaneous change in electronegativity among six iron atoms indicates a possible synergistic effect in complex **I** during the catalytic reaction.

The multimetal synergy behaviors are embodied not only in the synergetic electron transfer, but also in the synergetic spin variation. The spin density (defined as spin-up density minus spin-down density) distribution for all intermediates is shown in Fig. S21.† An antisymmetric spin polarization is observed in pristine complex **I** with Fe1, Fe2, Fe5 spin-up polarized and Fe3, Fe4, Fe6 spin-down polarized, which is the more stable coupled state in multinuclear complexes with a bridging oxo ligand.[19] After the deprotonation of bridging hydroxide, the spin polarization of Fe1 and Fe4 in **IV** exhibits a notable

increase compared to that of **I** and **II**, which is consistent with the $\Delta\rho$ distribution results discussed above. After the second deprotonation process of H_2O, a dramatic spin variation occurs on Fe1–Fe4; the antisymmetric spin polarization is broken, while Fe5 and Fe6 remain almost unchanged in **V**, **VI**, and **VII**. Conventional spin flip usually results in a large energy barrier; here, the spin variation of Fe1 is promoted *via* the synergistic behavior achieved by the electron transfer between multiple iron atoms, which is not accessible in mononuclear counterparts.[70]

Spin variation during the catalytic process can be more easily distinguished in the atomic magnetic moment (*m*) plots shown in Fig. 5f. Obviously, the deprotonation of bridging hydroxide leads to a dramatic increase in the spin polarization of Fe1 in IV compared with III. The higher spin polarization of Fe1 improves the electron transfer ability and reactivity, facilitating the catalytic process through the WNA mechanism.[68] Interestingly, as the spin polarization of Fe1 changes in different intermediates, that of the other three hexacoordinated Fe (Fe2, Fe3, and Fe4) changes correspondingly, while the spin polarizations of heptacoordinated Fe5 and Fe6 remain almost unchanged. Notably, Fe4 exhibits the opposite direction of spin polarization variation with a similar magnitude to Fe1, consistent with the $\Delta\rho$ distribution results discussed above. Specifically, when the spin polarization of Fe1 changes drastically, the total net spin polarization of the intermediates changes very little (green line in Fig. 5f) through the synergistic spin variation of other iron atoms. Such multimetal synergy, achieved in multinuclear catalysts to activate and promote catalytic reactions, is widespread in nature.[70] The reason for the cooperative spin variation of Fe1–Fe4 is probably that the four hexacoordinated Fe atoms have highly hybridized 3d-orbitals (Fig. 5a–d). The different bonding behaviors of Fe1 in different intermediates influence the hybridization between the orbitals of all four Fe atoms and lead to electron redistribution on the 3d-orbitals, as shown in the differential charge density distribution. It is also observed (Fig. S22†) that there are obvious spin redistributions on the different d-orbitals of Fe1–Fe4 during the deprotonation process. These iron atoms (Fe1–Fe4) jointly transfer electrons with the adsorbate ($-OH_2$, $-OH$, $-O$, and $-OOH$) to promote electron transfer, and thus keep the total spin state relatively stable during deprotonation processes. Therefore, the synergistic and electronic effects between multiple iron atoms in enhancing water oxidation activity are proven.

3   Conclusions

In this work, the hexanuclear iron(III) complex **I** was designed and the outstanding water oxidation performance of complex **I** under acidic conditions (pH 2 phosphate buffer) was verified. *In situ* spectroelectrochemistry provided direct experimental evidence of the key high-oxidation-state iron–oxo intermediates formed during the water oxidation process. On the basis of kinetics studies and DFT calculations, the WNA mechanism

was proposed as the reaction pathway of water oxidation by complex **I**.

Reversible proton transfer plays an important role in high-efficiency water oxidation. First, the deprotonation of bridging hydroxide can increase the electronegativity of the six iron atoms, and enhance spin polarization to activate the adsorbate and promote the reaction. Second, the significantly hybridized orbitals enhance the electron and proton transfer ability, and thus resulting in charge redistribution, which affects the bond strength, endowing complex **I** with outstanding catalytic performance. More importantly, the multimetal synergistic spin variation in the water oxidation process keeps the total spin polarization relatively stable, which is responsible for the high efficiency and stability of the catalyst. The present study investigated the roles of synergistic and electronic effects between metal centers in catalysis, which can provide a deeper understanding of the catalytic mechanism of water oxidation.

Data availability

All relevant data are within the manuscript and its Additional files. The data are available from the corresponding author on reasonable request.

Conflicts of interest

There are no conflicts to declare.

References

1 Y. Yuan, Z. Yu, D. Chen and Z. Zou, *Chem. Soc. Rev.*, 2017, **46**, 603–631.

2 B. Zhang and L. Sun, *Chem. Soc. Rev.*, 2019, **48**, 2216–2264.

3 J. D. Blakemore, R. H. Crabtree and G. W. Brudvig, *Chem. Rev.*, 2015, **115**, 12974–13005.

4 P. Garrido-Barros, C. Gimbert-Suriñach, R. Matheu, X. Sala and A. Llobet, *Chem. Soc. Rev.*, 2017, **46**, 6088–6098.

5 H. Dau and M. Haumann, *Coord. Chem. Rev.*, 2008, **252**, 273–295.

6 B. Lassalle-Kaiser, T. T. Boron, V. Krewald, J. Kern, M. A. Beckwith, M. U. Delgado-Jaime, H. Schroeder, R. Alonso-Mori, D. Nordlund, T.-C. Weng, D. Sokaras, F. Neese, U. Bergmann, V. K. Yachandra, S. DeBeer,

V. L. Pecoraro and J. Yano, *Inorg. Chem.*, 2013, **52**, 12915–12922.

7 T. J. Meyer, M. H. V. Huynh and H. H. Thorp, *Angew. Chem., Int. Ed.*, 2007, **46**, 5284–5304.

8 Q. Chen, Z. Cheng, R. Liao and M. Zhang, *J. Am. Chem. Soc.*, 2021, **143**, 19761–19768.

9 V. Kunz, M. Schulze, D. Schmidt and F. Würthner, *ACS Energy Lett.*, 2017, **2**, 288–293.

10 S. A. Bartlett, E. V. Sackville, E. K. Gibson, V. Celorrio, P. P. Wells, M. Nachtegaal, S. W. Sheehan and U. Hintermair, *Chem. Commun.*, 2019, **55**, 7832–7835.

11 X. Li, X. Zhang, M. Guo, B. Lv, K. Guo, X. Jin, W. Zhang, Y. Lee, S. Fukuzumi, W. Nam and R. Cao, *J. Am. Chem. Soc.*, 2021, **143**, 14613–14621.

12 Y. Su, W. Luo, W. Lin, Y. Su, Z. Li, Y. Yuan, J. Li, G. Chen, Z. Li, Z. Yu and Z. Zou, *Angew. Chem., Int. Ed.*, 2022, **61**, e202201430.

13 A. M. Geer, C. Musgrave III, C. Webber, R. J. Nielsen, B. A. McKeown, C. Liu, P. P. M. Schleker, P. Jakes, X. Jia, D. A. Dickie, J. Granwehr, S. Zhang, C. W. Machan, W. A. Goddard and T. B. Gunnoe, *ACS Catal.*, 2021, **11**, 7223–7240.

14 M. A. Khan, S. Khan, S. Sengupta, B. N. Mongal and S. Naskar, *Coord. Chem. Rev.*, 2024, **504**, 215679.

15 M. Blasco-Ahicart, J. Soriano-López, J. J. Carbó, J. M. Poblet and J. R. Galan-Mascaros, *Nat. Chem.*, 2018, **10**, 24–30.

16 T. Liu, B. Zhang and L. Sun, *Chem. – Asian J.*, 2019, **14**, 31–43.

17 M. Okamura, M. Kondo, R. Kuga, Y. Kurashige, T. Yanai, S. Hayami, V. K. K. Praneeth, M. Yoshida, K. Yoneda, S. Kawata and S. Masaoka, *Nature*, 2016, **530**, 465–468.

18 M. N. Akhtar, R. Bikas, M. A. AlDamen, Z. Shaghaghi, M. Shahid and A. Sokolov, *Dalton Trans.*, 2022, **51**, 12686–12697.

19 H. Zhang, X. Su, F. Xie, R. Liao and M. Zhang, *Angew. Chem., Int. Ed.*, 2021, **60**, 12467–12474.

20 X. Wei, T. Ding, Y. Wang, B. Yang, Q. Yang, S. Ye, C. Tung and L. Wu, *Angew. Chem., Int. Ed.*, 2023, **62**, e202308192.

21 P. Pelosin, M. Gil-Sepulcre, P. Garrido-Barros, D. Moonshiram, J. Benet-Buchholz, C. Gimbert-Suriñach and A. Llobet, *iScience*, 2020, **23**, 101378.

22 W. Micklitz and S. J. Lippard, *Inorg. Chem.*, 1988, **27**, 3067–3069.

23 W. Micklitz, S. G. Bott, J. G. Bentsen and S. J. Lippard, *J. Am. Chem. Soc.*, 1989, **111**, 372–374.

24 X. Zhang, H. Furutachi, S. Fujinami, S. Nagatomo, Y. Maeda, Y. Watanabe, T. Kitagawa and M. Suzuki, *J. Am. Chem. Soc.*, 2005, **127**, 826–827.

25 G. Hu, J. L. Troiano, U. T. Tayvah, L. S. Sharninghausen, S. B. Sinha, D. Y. Shopov, B. Q. Mercado, R. H. Crabtree and G. W. Brudvig, *Inorg. Chem.*, 2021, **60**, 14349–14356.

26 M. Kodera, M. Itoh, K. Kano, T. Funabiki and M. Reglier, *Angew. Chem., Int. Ed.*, 2005, **44**, 7104–7106.

27 J. R. Ferraro and W. R. Walker, *Inorg. Chem.*, 1965, **4**, 1382–1386.

28 D. Armentano, G. De Munno, T. F. Mastropietro, M. Julve and F. Lloret, *J. Am. Chem. Soc.*, 2005, **127**, 10778–10779.

29 D. N. Bowman, A. Bondarev, S. Mukherjee and E. Jakubikova, *Inorg. Chem.*, 2015, **54**, 8786–8793.

30 D. den Boer, Q. Siberie, M. A. Siegler, T. H. Ferber, D. C. Moritz, J. P. Hofmann and D. G. H. Hetterscheid, *ACS Catal.*, 2022, **12**, 4597–4607.

31 G. Weber, N. Von Wirén and H. Hayen, *Rapid Commun. Mass Spectrom.*, 2006, **20**, 973–980.

32 F. Miccichè, G. J. Long, A. M. Shahin, F. Grandjean, W. Ming, J. van Haveren and R. van der Linde, *Inorg. Chim. Acta*, 2007, **360**, 535–545.

33 C. Papatriantafyllopoulou, C. M. Kizas, M. J. Manos, A. Boudalis, Y. Sanakis and A. J. Tasiopoulos, *Polyhedron*, 2013, **64**, 218–230.

34 H. Oshio, N. Hoshino, T. Ito, M. Nakano, F. Renz and P. Gütlich, *Angew. Chem., Int. Ed.*, 2003, **42**, 223–225.

35 J. K. McCusker, C. A. Christmas, P. M. Hagen, R. K. Chadha, D. F. Harvey and D. N. Hendrickson, *J. Am. Chem. Soc.*, 1991, **113**, 6114–6124.

36 J. Qi, Y. Lin, D. Chen, T. Zhou, W. Zhang and R. Cao, *Angew. Chem., Int. Ed.*, 2020, **59**, 8917–8921.

37 D. Wang and J. T. Groves, *Proc. Natl. Acad. Sci. U. S. A.*, 2013, **110**, 15579–15584.

38 P. Karuppasamy, D. Thiruppathi, M. Ganesan, T. Rajendran, S. Rajagopal, V. K. Sivasubramanian and V. Rajapandian, *Electrocatalysis*, 2021, **12**, 516–536.

39 A. E. M. Boelrijk, S. V. Khangulov and G. C. Dismukes, *Inorg. Chem.*, 2000, **39**, 3009–3019.

40 J. B. Gerken, J. G. McAlpin, J. Y. C. Chen, M. L. Rigsby, W. H. Casey, R. D. Britt and S. S. Stahl, *J. Am. Chem. Soc.*, 2011, **133**, 14431–14442.

41 K. R. Gorantla and B. S. Mallik, *Dalton Trans.*, 2022, **51**, 11899–11908.

42 W.-P. To, T. W.-S. Chow, C.-W. Tse, X. Guan, J.-S. Huang and C.-M. Che, *Chem. Sci.*, 2015, **6**, 5891–5903.

43 Q. Chen, Y. Xiao, R. Liao and M. Zhang, *CCS Chem.*, 2023, **5**, 245–256.

44 M. Zhang, Z. Chen, P. Kang and T. J. Meyer, *J. Am. Chem. Soc.*, 2013, **135**, 2048–2051.

45 H. Yang, F. Li, S. Zhan, Y. Liu, W. Li, Q. Meng, A. Kravchenko, T. Liu, Y. Yang, Y. Fang, L. Wang, J. Guan, I. Furó, M. S. G. Ahlquist and L. Sun, *Nat. Catal.*, 2022, **5**, 414–429.

46 L. L. Williams and R. D. Webster, *J. Am. Chem. Soc.*, 2004, **126**, 12441–12450.

47 M. Kondo, H. Tatewaki and S. Masaoka, *Chem. Soc. Rev.*, 2021, **50**, 6790–6831.

48 B. Zhang, F. Li, F. Yu, H. Cui, X. Zhou, H. Li, Y. Wang and L. Sun, *Chem. – Asian J.*, 2014, **9**, 1515–1518.

49 H. Dau, C. Limberg, T. Reier, M. Risch, S. Roggan and P. Strasser, *ChemCatChem*, 2010, **2**, 724–761.

50 V. Artero and M. Fontecave, *Chem. Soc. Rev.*, 2013, **42**, 2338–2356.

51 K. J. Lee, B. D. McCarthy and J. L. Dempsey, *Chem. Soc. Rev.*, 2019, **48**, 2927–2945.

52 J. E. Tackett, *Appl. Spectrosc.*, 1989, **43**, 490–499.

53 G. Chen, L. Chen, S. Ng, W. Man and T. Lau, *Angew. Chem., Int. Ed.*, 2013, **52**, 1789–1791.

54 D. Hong, S. Mandal, Y. Yamada, Y.-M. Lee, W. Nam, A. Llobet and S. Fukuzumi, *Inorg. Chem.*, 2013, **52**, 9522–9531.

55 H. Du, S. Chen, X. Su, L. Jiao and M. Zhang, *J. Am. Chem. Soc.*, 2018, **140**, 1557–1565.

56 R. Matheu, S. Neudeck, F. Meyer, X. Sala and A. Llobet, *ChemSusChem*, 2016, **9**, 3361–3369.

57 Y. Zhao, X. F. Lu, Z. Wu, Z. Pei, D. Luan and X. W. (David) Lou, *Adv. Mater.*, 2023, **35**, 2207888.

58 S. I. Shylin, M. V. Pavliuk, L. D'Amario, F. Mamedov, J. Sá, G. Berggren and I. O. Fritsky, *Chem. Commun.*, 2019, **55**, 3335–3338.

59 Q. Huang, S. Xie, J. Hao, Z. Ding, C. Zhang, H. Sheng and J. Zhao, *Angew. Chem., Int. Ed.*, 2023, **62**, e202300469.

60 D. D. Boer, A. I. Konovalov, M. A. Siegler and D. G. H. Hetterscheid, *Inorg. Chem.*, 2023, **62**, 5303–5314.

61 W. C. Ellis, N. D. McDaniel, S. Bernhard and T. J. Collins, *J. Am. Chem. Soc.*, 2010, **132**, 10990–10991.

62 S. D'Agostini, K. G. Kottrup, C. Casadevall, I. Gamba, V. Dantignana, A. Bucci, M. Costas, J. Lloret-Fillol and D. G. H. Hetterscheid, *ACS Catal.*, 2021, **11**, 2583–2595.

63 A. I. Nguyen, M. S. Ziegler, P. Oña-Burgos, M. Sturzbecher-Hohne, W. Kim, D. E. Bellone and T. D. Tilley, *J. Am. Chem. Soc.*, 2015, **137**, 12865–12872.

64 H. Dau, L. Iuzzolino and J. Dittmer, *Biochim. Biophys. Acta*, 2001, **1503**, 24–39.

65 J. Song, C. Wei, Z. Huang, C. Liu, L. Zeng, X. Wang and Z. J. Xu, *Chem. Soc. Rev.*, 2020, **49**, 2196–2214.

66 Z. Zhang, P. Ma, L. Luo, X. Ding, S. Zhou and J. Zeng, *Angew. Chem., Int. Ed.*, 2023, **62**, e202216837.

67 A. Vojvodic and J. K. Nørskov, *Science*, 2011, **334**, 1355–1356.

68 H. Bai, J. Feng, D. Liu, P. Zhou, R. Wu, C. T. Kwok, W. F. Ip, W. Feng, X. Sui, H. Liu and H. Pan, *Small*, 2022, **19**, 2205638.

69 M. Haumann, C. Müller, P. Liebisch, L. Iuzzolino, J. Dittmer, M. Grabolle, T. Neisius, W. Meyer-Klaucke and H. Dau, *Biochemistry*, 2005, **44**, 1894–1908.

70 A. C. Ghosh, C. Duboc and M. Gennari, *Coord. Chem. Rev.*, 2021, **428**, 213606.